Dynamics of uS19 C-Terminal Tail during the Translation Elongation Cycle in Human Ribosomes

Varun Bhaskar, Alexandra Graff-Meyer, Andreas Schenk, Simone Cavadini, Ottilie von Loeffelholz, S. Kundhavai Natchiar, Caroline Artus-Revel, Hans-Rudolf Hotz, Gabriel Bretones, Bruno Klaholz, et al.

Dynamics of uS19 C-Terminal Tail during the Translation Elongation Cycle in Human Ribosomes

Graphical Abstract
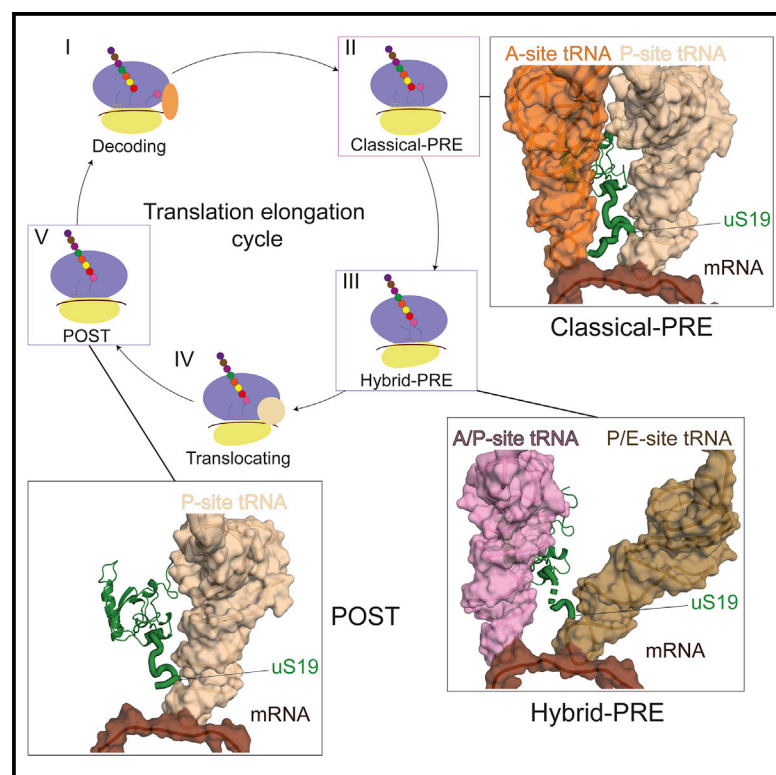
Authors

Varun Bhaskar, Alexandra Graff-Meyer, Andreas D. Schenk, ..., Gabriel Bretones, Bruno P. Klaholz, Jeffrey A. Chao

Correspondence

jeffrey.chao@fmi.ch

In Brief

In this study, Bhaskar et al. visualize the dynamic rearrangement of the uS19 C-terminal tail during translation elongation and elucidate its role in stabilizing aminoacyl tRNA and decoding interactions and in coordination of peptidyl tRNA movements within the mammalian ribosome during protein synthesis.

Highlights

- uS19 C-terminal tail undergoes dynamic rearrangement during translation elongation

- uS19 C-terminal tail stabilizes the P-site tRNA and decoding interactions

- Disease-associated mutations in uS19 C-terminal tail cause translational defects

CellPress

Dynamics of uS19 C-Terminal Tail during the Translation Elongation Cycle in Human Ribosomes

Varun Bhaskar,[1] Alexandra Graff-Meyer,[1] Andreas D. Schenk,[1] Simone Cavadini,[1] Ottilie von Loeffelholz,[2,3,4,5,6] S. Kundhavai Natchiar,[2,3,4,5,6] Caroline G. Artus-Revel,[1] Hans-Rudolf Hotz,[1] Gabriel Bretones,[7] Bruno P. Klaholz,[2,3,4,5,6] and Jeffrey A. Chao[1,8,*]

[1]Friedrich Miescher Institute for Biomedical Research, 4058 Basel, Switzerland
[2]Centre for Integrative Biology (CBI), Department of Integrated Structural Biology, IGBMC, CNRS, INSERM, Université de Strasbourg, 1 rue Laurent Fries, 67404 Illkirch, France
[3]Institute of Genetics and of Molecular and Cellular Biology (IGBMC), 1 rue Laurent Fries, Illkirch, France
[4]Centre National de la Recherche Scientifique (CNRS), UMR 7104, Illkirch, France
[5]Institut National de la Santé et de la Recherche Médicale (INSERM), U964, Illkirch, France
[6]Université de Strasbourg, Illkirch, France
[7]Departamento de Bioquímica y Biología Molecular, Instituto Universitario de Oncología del Principado de Asturias (IUOPA), Universidad de Oviedo, 33006 Oviedo, Spain
[8]Lead Contact
*Correspondence: jeffrey.chao@fmi.ch
https://doi.org/10.1016/j.celrep.2020.03.037

SUMMARY

Ribosomes undergo multiple conformational transitions during translation elongation. Here, we report the high-resolution cryoelectron microscopy (cryo-EM) structure of the human 80S ribosome in the post-decoding pre-translocation state (classical-PRE) at 3.3-Å resolution along with the rotated (hybrid-PRE) and the post-translocation states (POST). The classical-PRE state ribosome structure reveals a previously unobserved interaction between the C-terminal region of the conserved ribosomal protein uS19 and the A- and P-site tRNAs and the mRNA in the decoding site. In addition to changes in the inter-subunit bridges, analysis of different ribosomal conformations reveals the dynamic nature of this domain and suggests a role in tRNA accommodation and translocation during elongation. Furthermore, we show that disease-associated mutations in uS19 result in increased frameshifting. Together, this structure-function analysis provides mechanistic insights into the role of the uS19 C-terminal tail in the context of mammalian ribosomes.

INTRODUCTION

Ribosomes are the molecular machines that are at the heart of protein synthesis. During the translation cycle, ribosomes adopt a series of distinct structural conformations that enable the information encoded within mRNAs to be translated into polypeptides (Agrawal et al., 1999; Anger et al., 2013; Behrmann et al., 2015; Budkevich et al., 2014; Frank and Agrawal, 2000; Khatter

et al., 2015; Natchiar et al., 2017; Shao et al., 2016; Spahn et al., 2004; Stark et al., 1997; Voorhees et al., 2014). This coordinated series of structural rearrangements is conserved in all kingdoms and begins with decoding the A-site codon by the EF-Tu/eEF1A-tRNA complex (decoding state) (Behrmann et al., 2015; Blanchard et al., 2004a; Green and Noller, 1997; Li et al., 2008; Pape et al., 1998; Rodnina and Wintermeyer, 2001a; Schmeing et al., 2009; Shao et al., 2016; Voorhees et al., 2010; Zaher and Green, 2009). After a successful decoding event, the elongation factor dissociates and the tRNA is accommodated into the A-site in the large subunit, resulting in the formation of the classical pre-translocation state (classical-PRE) with the tRNAs in classical conformation (A/A and P/P) and transfer of nascent chain to the A-site tRNA (Behrmann et al., 2015; Blanchard et al., 2004a; Jenner et al., 2010; Rodnina and Wintermeyer, 2001b; Voorhees et al., 2009; Whitford et al., 2010; Zaher and Green, 2009). Subsequently, the ribosome attains a ratcheted conformation (hybrid-PRE) with the tRNAs in a hybrid conformation (A/P and P/E) due to translocation of the large subunit (Behrmann et al., 2015; Blanchard et al., 2004b; Cornish et al., 2008; Frank and Agrawal, 2000; Moazed and Noller, 1989; Voorhees et al., 2014). This is followed by binding of EF-G/eEF2, which stabilizes the complex, prevents the P-site tRNA from frame shifting (Zhou et al., 2019), and helps to resolve the ratcheted state of the ribosome and translocation of the small subunit (Agrawal et al., 1999; Anger et al., 2013; Frank and Agrawal, 2000; Moazed and Noller, 1989; Rodnina et al., 1997; Spiegel et al., 2007; Valle et al., 2003; Wintermeyer and Rodnina, 2000). After translocation, EF-G/eEF2 dissociates from the ribosome, leading to formation of the post-translocated state (POST state) with an empty A-site and the P- and E-site tRNAs in classical conformation that is ready for the next round of decoding.

Although the overall features of translation elongation are highly conserved across all kingdoms of life (Agrawal et al., 1999; Frank and Agrawal, 2000; Moazed and Noller, 1989;
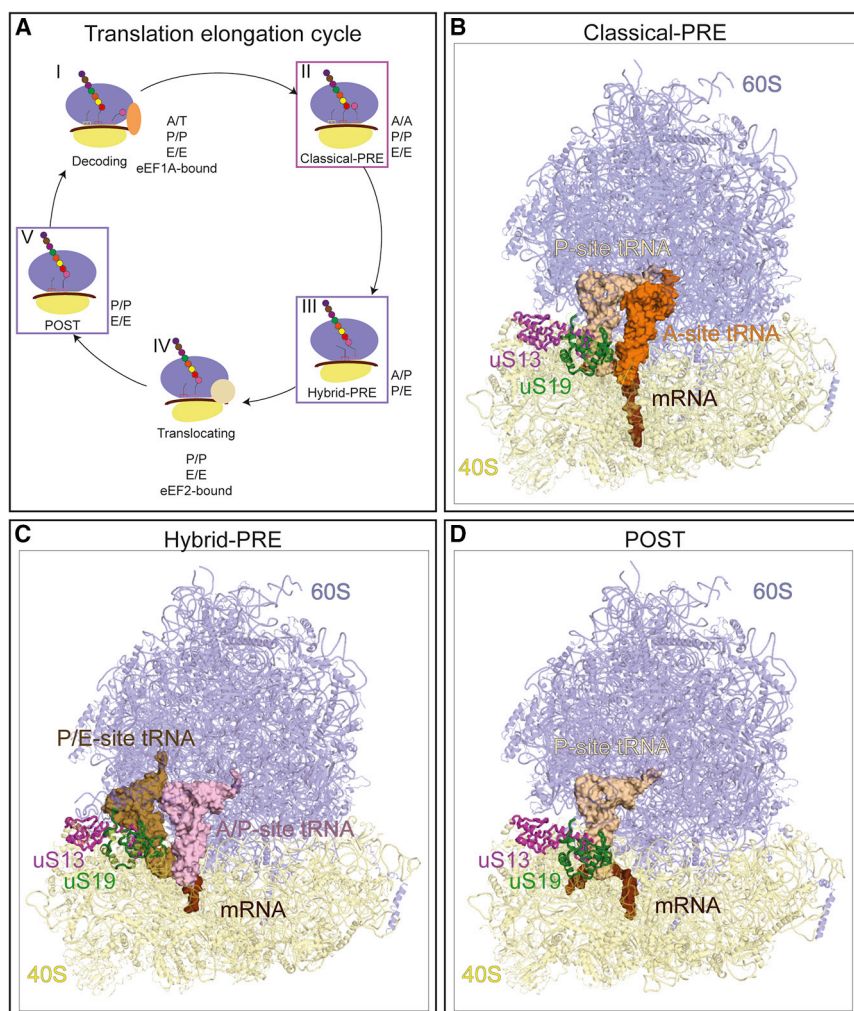
Figure 1. Distinct Conformations of Human Ribosomes Observed during the Translation Elongation Cycle

(A) Overview of eukaryotic translation elongation cycle. The classical-PRE conformation is indicated by a magenta box, and the hybrid-PRE and POST conformations are indicated by violet boxes.
(B–D) Structures of the active human ribosome in classical-PRE (B), hybrid-PRE (C), and POST (D) conformations. Large (60S, blue) and small (40S, yellow) subunits are shown with uS13 (magenta), uS19 (green), mRNA (brown), A-site (orange), P-site (wheat), A/P-site (pink), and P/E-site (sand) tRNAs.

in coordinating P-site tRNA movement with ribosomal subunit rotation during elongation. The C-terminal tail of uS19 is highly conserved in eukaryotes and archaea, mutations in this region correlate with aggressive forms of chronic lympho-cytic leukemia (CLL), and its phosphoryla-tion is increased in Parkinson disease (Bretones et al., 2018; Landau et al., 2015; Ljungström et al., 2016; Martin et al., 2014; Yu et al., 2017). The struc-tures of the human ribosome in the clas-sical-PRE and hybrid-PRE states provide not only a structural framework for under-standing the molecular basis for distinct intermediate states occurring in the hu-man ribosome during elongation but also for their dysregulation in diseases. Finally, an analysis of the interface be-tween the 40S and 60S subunits in the classical-PRE and the POST states sheds light on the distinct inter-subunit bridges

Rodnina et al., 1997; Spiegel et al., 2007; Valle et al., 2003; Wintermeyer and Rodnina, 2000), several variations, such as mammalian-specific subunit rolling, have evolved in higher eu-karyotes (Budkevich et al., 2014). Recently, high-resolution sin-gle-particle cryoelectron microscopy (cryo-EM) structures of mammalian ribosomes have enabled the visualization of multi-ple intermediate states of ribosomes during elongation, including the decoding state and the hybrid-PRE and the POST states (Anger et al., 2013; Behrmann et al., 2015; Khatter et al., 2015; Natchiar et al., 2017; Shao et al., 2016). These structures have contributed toward a more detailed mecha-nistic understanding of mammalian protein synthesis. Yet, within the mammalian translation cycle, a high-resolution struc-ture of the classical-PRE state, a key intermediate that forms post-decoding and following eEF1A dissociation, has remained elusive.

Here, we report structures of the human ribosome in the clas-sical-PRE state along with the hybrid-PRE and the POST states. A comparison of the ribosomes in these three distinct conforma-tions shows that the C-terminal tail of uS19 (RPS15) stabilizes A-site tRNA decoding interactions and points to its contribution

present in these states. Together, these results highlight the function of the uS19 C-terminal tail in the context of mammalian ribosomes.

RESULTS

The C-Terminal Tail of uS19 Stabilizes the P- and A-Site tRNAs and Decoding Interactions in the Classical-PRE State Ribosome

We isolated translating ribosomes from HEK293 cells in the pres-ence of cycloheximide for single-particle cryo-EM analysis. The 2D and 3D classifications of the cryo-EM datasets collected on this sample revealed the presence of ribosomes predominantly in three conformations: the classical-PRE state, the hybrid-PRE state, and the POST state (Figures 1A–1D, S1, and S2; Table S1). The two structures of human ribosomes in the hybrid-PRE and the POST states found in this study are similar to the conformational states of the previously reported porcine and human ribosomes (Behrmann et al., 2015; Khatter et al., 2015; Natchiar et al., 2017; Voorhees et al., 2014). In addition, we obtained a high-resolution structure of the classical-PRE
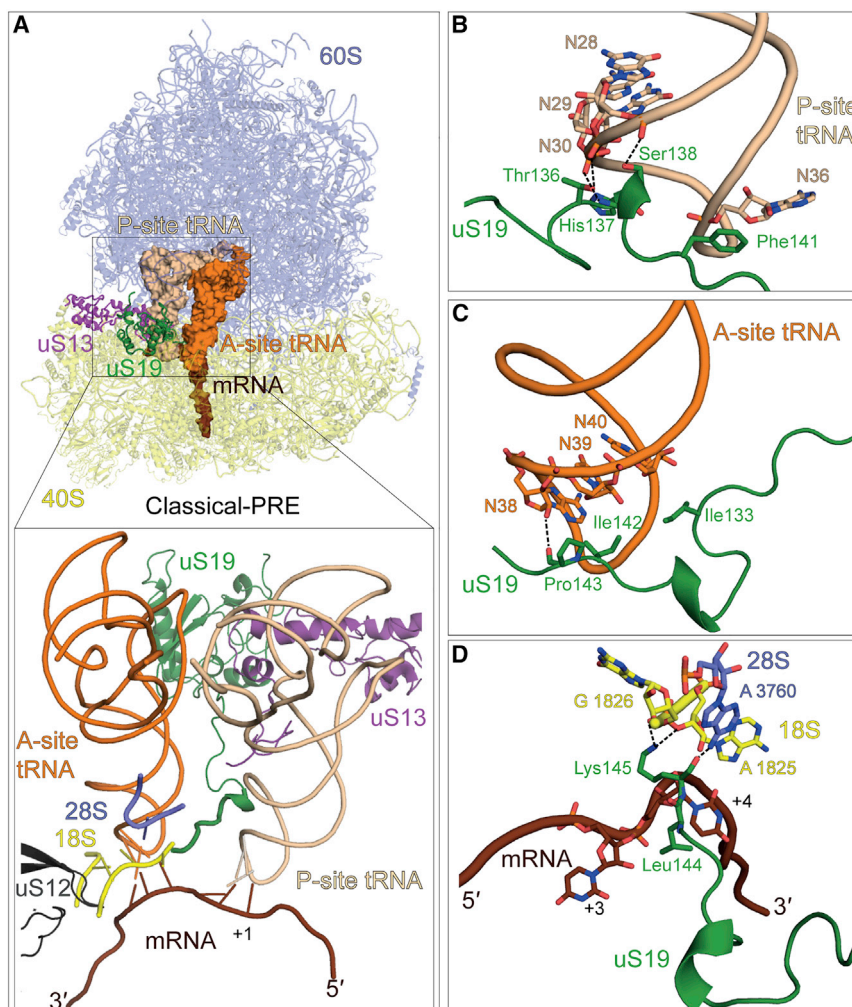
Figure 2. uS19 C-Terminus-Mediated Stabilization of the Decoding Center in the Classical-PRE Conformation

(A) Structure of the human ribosome in the classical-PRE conformation and close-up view of the decoding center. Region of uS12 (residues 54–69, black) close to the decoding site with uS13 (magenta) and uS19 (green).

(B–D) Interactions of the C-terminal tail of uS19 (green) with the P-site tRNA (B, wheat), the A-site tRNA (C, orange), and the mRNA (D, brown). Regions of h44 of 18S rRNA (yellow) and H69 of 28S rRNA (blue) are also shown. Polar interactions are denoted by dotted lines.

state mammalian ribosome that contains the 40S subunit in a rolled conformation bound to A- and P-site tRNAs in the classical positions (A/A and P/P, rather than A/P and P/E intermediates) (Figure 1B).

In the human classical-PRE state ribosome, we observe all the interactions of universally conserved A1824, A1825 (of helix h44), and G560 of the 18S rRNA and A3760 (of helix H69) of the 28S rRNA with the codon-anticodon pairs (Figure 2A). Additionally, we detected an unaccounted map density between the A- and P-site tRNAs that extended into the decoding center. The well-resolved features of the map enabled an unambiguous amino acid sequence assignment and atomic model building of the distal C-terminal tail of ribosomal protein uS19 (residues 136–145) (Figures 2A and S3A). The C-terminal tail of uS19 consists of residues 128–145 that can be divided into a proximal region (residues 128–135) interacting predominantly with the 18S rRNA and a distal region (residues 136–145) positioned between the A- and P- site tRNAs. This distal region of the uS19 tail has not been fully visualized in previous 80S ribosome structures, but its location in the classical-PRE state is consistent with crosslinking studies that detected an interaction between

Lys145 of uS19 and components of the decoding center (Pisarev et al., 2008).

The uS19 C-terminal tail was found to interact with the A- and P-site tRNAs, rRNA helices h44 and H69, as well as the +4 position of the mRNA (+1 position being the first nucleotide of the codon in the P-site). The interaction between the uS19 C-terminal tail and the P-site tRNA is mediated by residues 136–141 that bind to the anticodon stem loop of the P-site tRNA (Figures 2B and S3B). This interface is dominated by hydrogen bonds between Thr136, His137, and Ser138 of uS19 and the phosphate groups of the N28, N29, and N30 nucleotides of the P-site tRNA. The precise identity of the nucleotides could not be determined because the ribosomes were isolated from cellular extracts and contain a mixture of tRNAs. Additionally, the aromatic ring of Phe141 of uS19

partially stacks against the ribose of N36. The anticodon stem of the A-site tRNA is also recognized by uS19 (Figures 2C and S3C). Hydrophobic contacts are made by side chains of Ile133 and Ile142 with the riboses of N40 and N39, respectively. Additionally, the backbone carbonyl of Pro143 forms a hydrogen bond with the 2′ OH of the ribose of N38. In the context of uS19-mRNA interactions, uS19 inserts the side chain of Leu144 between the +3 and +4 nucleotides of the mRNA to shield the codon-anticodon base-pairing interactions at this position (Figures 2D and S3D). Furthermore, the side chain of Lys145 is involved in a hydrophobic contact with the ribose of the +4 nucleotide of the mRNA (Figure 2D). Lys145 also forms additional interactions with the extruded nucleotides A3760 of helix H69 and G1826 of helix h44 (Figures 2D and S3D). It is important to note that the interactions of the uS19 C-terminal tail with the mRNA or A-site tRNA are not observed in the eEF1A-bound decoding state (Shao et al., 2016). Therefore, the stabilization of decoding interactions by the uS19 C-terminal tail suggests a role in efficient accommodation of A-site tRNA post eEF1A dissociation and kinetic proofreading of the decoded tRNA.
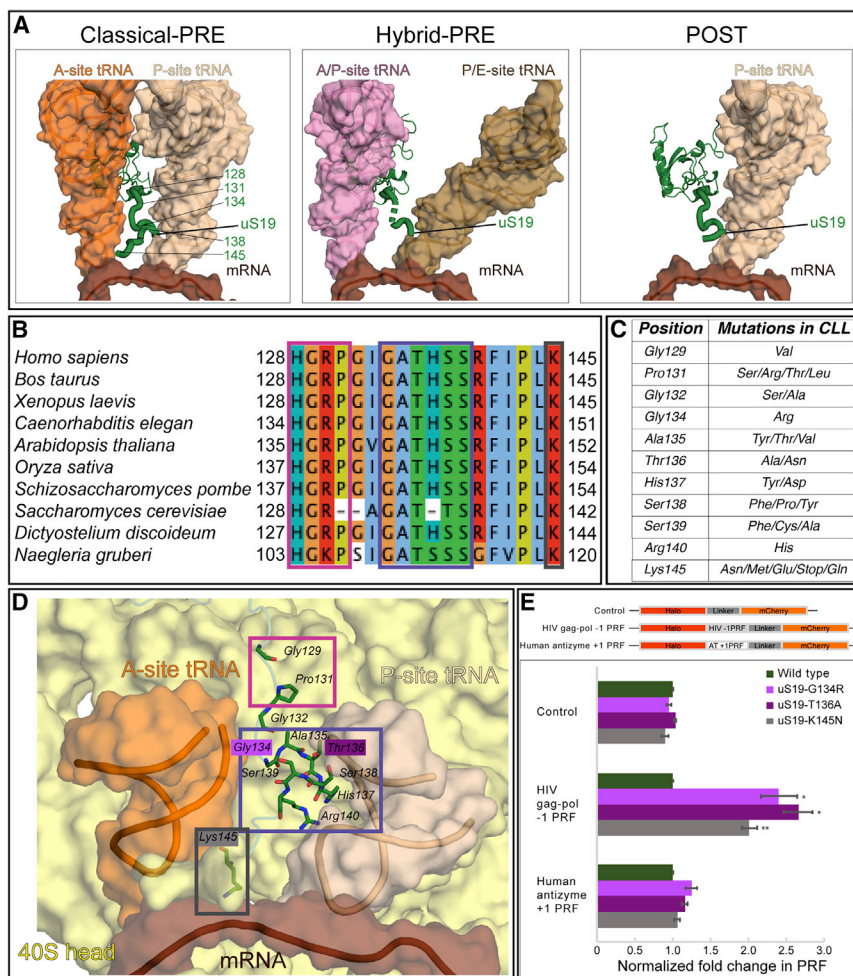
Figure 3. Interactions and Disease-Associated Mutations of uS19 C-Terminal Tail

(A) Position of the uS19 (green) C-terminal tail with respect to tRNAs in classical-PRE state, hybrid-PRE, and POST states are shown. mRNA (brown), A-site (orange), A/P hybrid (pink), P-site (wheat), and P/E hybrid tRNAs (sand) are displayed as surfaces.

(B) Representative sequence alignment of the C-terminal tail of uS19 from eukaryotes. The hinge regions are indicated by colored boxes.

(C) Mutations found in the CLL cluster in the C-terminal tail of uS19.

(D) Position of the uS19 C-terminal tail within the decoding center. The hinge regions are indicated by colored boxes. Residues that are frequently mutated in case of CLL are represented as sticks.

(E) uS19 mutations increase PRF. Schematic of dual-fluorescent reporter constructs for PRF based on HIV-1 gag-pol and human antizyme 1 genes and quantification of PRF for uS19 C-terminal tail mutations. The error bars represent standard error of mean.

Position	Mutations in CLL
Gly129	Val
Pro131	Ser/Arg/Thr/Leu
Gly132	Ser/Ala
Gly134	Arg
Ala135	Tyr/Thr/Val
Thr136	Ala/Asn
His137	Tyr/Asp
Ser138	Phe/Pro/Tyr
Ser139	Phe/Cys/Ala
Arg140	His
Lys145	Asn/Met/Glu/Stop/Gln

The C-Terminal Tail of uS19 Undergoes a Dynamic Rearrangement during Translation Elongation

The structure of the classical-PRE state ribosome shows that the C terminus of uS19 (residues 128–145) is highly ordered in this conformation (Figures 2A and S3). In contrast to the classical-PRE state, residues Gly132 and Ile133 of the uS19 C-terminal tail become disordered in the hybrid-PRE state (Figure 3A). Furthermore, residues Thr136 and His137 move with the P-site tRNA to contact the P/E tRNA during ribosomal subunit rotation (Figure 3A). The flexibility of Gly132 could be essential for the maintenance of stable interactions between the uS19 C-terminal tail and P/E tRNAs. Additionally, conformational changes in the P-site tRNA and swiveling of the head domain of the 40S subunit to form the hybrid-PRE conformation lead to the detachment of the C-terminal tail from the 28S rRNA, A-site tRNA and the A-site codon-anticodon stem. As a result, residues between 138 and 145 are disordered (Figure 3A). Similarly, in the POST state, the C-terminal tail of uS19 is only ordered until residue 139 (Figure 3A). The coordinated change in conformation of the uS19 C-terminal tail and P-site tRNA in the classical-PRE, hybrid-PRE, and the POST states suggests its contribution toward stabilization of the P-site tRNA during translation elongation.

Based on these data, we propose a two-hinge and a latch model for the function of the C-terminal tail of uS19 during elongation. Specifically, the first hinge (residues 128–131) holds the tail in the proximal region of the A- and P-site tRNAs and the decoding site by anchoring the tail onto the 18S rRNA, which is maintained throughout the translation cycle. The second hinge, residues 134–139, functions to stabilize and coordinate the movement of the P-site tRNA. The region between these two hinge points (residues 132–133) may entail flexibility to accommodate the conformational changes of the P-site tRNA during elongation. Residues 143–145 interact with the A-site tRNA and the mRNA at the decoding site and act as a final latch point that may contribute to efficient accommodation of the A-site tRNA.

Insights into Disease-Associated Mutations of the uS19 C-Terminal Tail

Mutations in the conserved uS19 C-terminal tail and its increased phosphorylation have been observed in CLL and Parkinson disease, respectively (Figures 3B and 3C; Bretones et al., 2018; Landau et al., 2015; Ljungström et al., 2016; Yu et al., 2017). These mutations alter translation rates and fidelity in these diseases and cluster predominantly within three regions of the uS19 C-terminal tail. One region is within the first hinge position (Gly129 and Pro131) that anchors the uS19 C-terminal tail during the translation elongation cycle (Figures 3A and 3D). Also, mutation of Gly132 could affect the dynamic nature of the tail during the transition from the classical-PRE to the hybrid-PRE state. Many of the uS19 C-terminal tail mutations cluster within the second hinge region (Gly134, Ala135, Thr136, His137, Ser138, and

Ser139), which contains residues that make critical interactions with the P-site tRNA (Figures 3A and 3D). Mutations in this region were also found to have the largest effects on amino acid mis-incorporation and stop codon read-through (Bretones et al., 2018). Interestingly, several members of *Thermoprotei*, a class composed of predominantly thermophilic archaebacteria, have a Lys in the position equivalent to Gly134, which is similar to the Gly134Arg mutation observed in CLL (Figures 3B, 3C, and S4). Finally, mutations in the latch region at the distal position of uS19 C-terminal tail (Lys145) could affect the stability of de-coding interactions during accommodation (Figures 3A–3D). Although most of these mutations either decrease or have no effect on the global rate of translation, the increased phosphor-ylation of Thr136 by a mutant of the leucine-rich repeat kinase 2 (LRRK2) in Parkinson disease leads to increased protein produc-tion (Bretones et al., 2018; Martin et al., 2014). These observa-tions support a function for uS19 in modulating the rate and fidelity of translation under normal physiological and disease conditions.

To investigate the consequence of uS19 C-terminal tail muta-tions on reading frame maintenance, we characterized their ef-fects on programmed ribosomal frameshifts (PRFs) by using dual-fluorescent reporters containing two different PRF se-quences (Figure 3E). One reporter contained a region of the HIV gag-pol gene that contains the slippery sequence and the downstream pseudo-knot sequence that leads to a −1 frame-shift (Harger and Dinman, 2003; Jacks et al., 1988). This PRF is thought to occur by tRNA slippage either during translocation or accommodation (Harger and Dinman, 2003; Jacks et al., 1988). The second reporter contained the PRF from human anti-zyme 1, where cellular concentrations of polyamines mediate a +1 frameshift of human antizyme 1 through occlusion of the first base of the A-site tRNA without necessarily involving tRNA slippage in mammals (Kurian et al., 2011; Matsufuji et al., 1995). In HEK293 cells, mutations of the second hinge region (Gly134Arg and Thr136Ala) and the latch region (Lys145Asn) re-sulted in an ~2.5-fold increase in HIV −1 PRF compared with the wild-type cells (Figure 3E). In comparison, the antizyme +1 sequence did not alter PRF. The increased HIV −1 PRF observed for the uS19 C-terminal tail mutants suggests a contribution of this region toward the maintenance of the reading frame during translation elongation.

Remodeling of Inter-subunit Bridges during the Transition from POST to Classical-PRE states

In mammals, A-site tRNA accommodation after eEF1A dissoci-ation is coupled to rolling of the 40S subunit toward the A-site by ~5° along the long axis (Figure 4A), which contributes to re-modeling of many inter-subunit bridges (Figures 4B and 4C). Although there are minimal changes in the conformation of the small subunit (SSU) between the POST and decoding states (Figure 4A), some inter-subunit bridges in the POST and the classical-PRE states differ (e.g., bridges B6 and B8 are present only in the classical-PRE state) (Figures 4B and 4C; Table S2). Additionally, in contrast to the POST state, bridges eB8, eB8b, and eB9 are not seen in the classical-PRE state, all of which are located adjacent to the E-site of the SSU (Figures 4B and 4C; Table S2). This results in widening

of the E-site by ~5 Å (calculated between G4371 of 28S and G970 of 18S), thereby facilitating the release of deacylated tRNA. Additionally, the width of the factor binding site is reduced by ~6 Å (calculated between G4600 of 28S and A464 of 18S), favoring efficient accommodation of the A-site tRNA. Additionally, we suggest that the remodeling of inter-subunit interactions could affect the stabilities of the clas-sical-PRE and POST states. Indeed, a previous study has showed that the classical-PRE state of human ribosomes is metastable compared with other states (Ferguson et al., 2015), and this could be a direct consequence of changes in in-ter-subunit interactions.

DISCUSSION

The classical-PRE state human ribosome structure contains A- and P-site tRNAs in the classical conformation and reveals the complete structure of the C-terminal tail of ribosomal protein uS19. Accommodation of aminoacyl tRNA in the A-site has been shown to be one of the rate limiting steps in translation (Blanchard et al., 2004a; Rodnina and Wintermeyer, 2001b; Whitford et al., 2010; Wohlgemuth et al., 2010). In this study, we show that the uS19 C-terminal tail stabilizes the interactions in the heart of the decoding center by providing additional inter-actions. This suggests a role of the uS19 C-terminal tail in effi-cient accommodation of A-site tRNA, which could contribute to kinetic proofreading post-decoding. Interestingly, the C-ter-minal tail of uS19 is conserved in eukaryotes and archaea but not in bacteria, with the exception of some bacteria, such as *Thermus thermophilus* where the C-terminal tail of uS13 appears to take over a similar function (Selmer et al., 2006; Shao et al., 2016). However, in eukaryotes, this interaction has become much more extensive between the P-site tRNA and uS19 C-ter-minal tail (buried surface area of 267 Å^2 in eukaryotes versus 77 Å^2 in bacteria).

During translation, it is essential to coordinate the move-ment of tRNAs during elongation to ensure the maintenance of the correct reading frame. The structures presented here provide insights into the mechanism by which uS19 interacts with the tRNAs in different ribosomal states. Specifically, we show that the uS19 C-terminal tail adopts distinct conforma-tions in the classical-PRE, hybrid-PRE, and POST states. These specific conformations of the uS19 C-terminal tail can be attributed to its unique architecture that contains distinct A- and P-site tRNAs and mRNA and 18S rRNA interacting re-gions with interspersed flexible regions. This enables it to maintain stable interactions with tRNAs to preserve the correct reading frame during translation, as illustrated by our PRF ex-periments that used uS19 mutants. Previously, it was reported that additional residues within uS19 participate in stabilizing the B1a inter-subunit bridge and mutations in these regions are also associated with increased PRF (Bowen et al., 2015). Our functional data supports a role of uS19 in coordinating tRNA movement with ribosomal inter-subunit rotation during translation elongation.

Our structural analysis of human ribosomes in the classical-PRE and POST states shows that during aminoacyl tRNA ac-commodation structural rearrangements occur due to rolling of
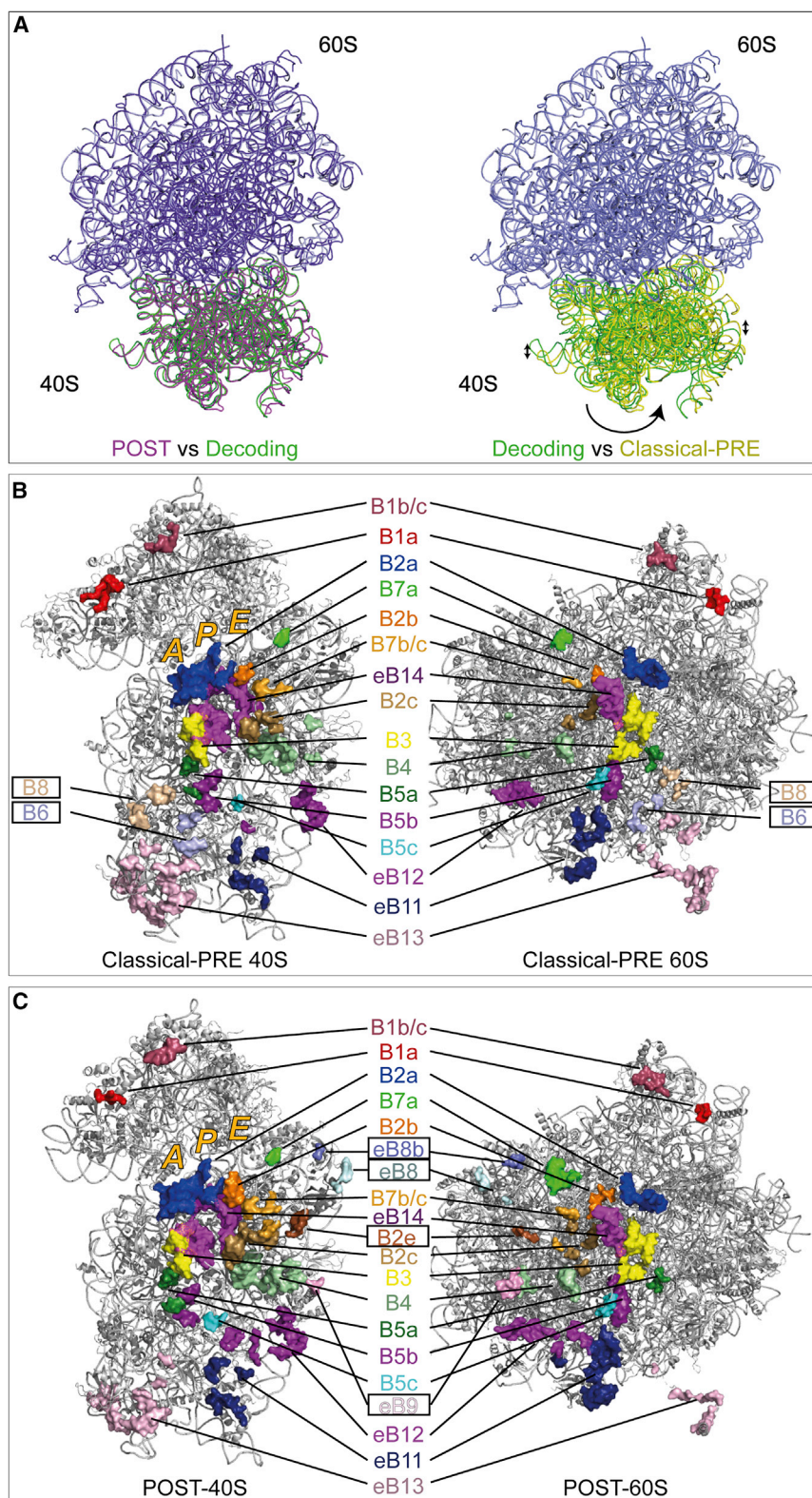
Figure 4. Remodeling of Inter-subunit Bridges Due to Rolling of the 40S Subunit

(A) Position of the 40S relative to the 60S subunit (only 18S and 28S rRNA are shown for clarity) in POST (magenta and purple), decoding (green and light blue) (PDB: 5LZS), and the classical-PRE (yellow and blue) states. The position of 40S in the decoding and POST states are similar compared with the position of 40S in the classical-PRE state.

(B) Regions of the 40S and 60S subunits contributing to inter-subunit bridges observed in the classical-PRE state ribosomes.

(C) Regions of the 40S and 60S subunits contributing to inter-subunit bridges observed in the POST state ribosomes. The bridges that are unique to each state are boxed.

the SSU. This could enhance aminoacyl tRNA accommodation and facilitate subsequent translocation that may lead to the maintenance of optimal translational rates. In this mammalian-specific context, we speculate that the function of the uS19 C-terminal tail becomes important, as it has to maintain stable interactions with the aminoacyl tRNA during subunit rolling to reduce the frequency of frame shifting and stochastic dissociation of aminoacyl tRNA during its accommodation.

Together, this first visualization of the mammalian ribosome in the classical PRE-state at high resolution defines a crucial intermediate, which fills a key gap in the mammalian translation elongation cycle. Furthermore, the insights provided here contribute to our understanding of the dynamic rearrangement of the uS19 C-terminal tail and support its role in facilitating aminoacyl tRNA accommodation and coordinated peptidyl tRNA movements within the mammalian ribosome during protein synthesis. In addition, our findings are also relevant for understanding the molecular basis of translational defects arising from uS19 mutations in human diseases.

STAR★METHODS

Detailed methods are provided in the online version of this paper and include the following:

- KEY RESOURCES TABLE
- LEAD CONTACT AND MATERIALS AVAILABILITY
- EXPERIMENTAL MODEL AND SUBJECT DETAILS
- METHOD DETAILS
  - Sample preparation
  - Image acquisition and data processing
  - Refinement and model building
  - Programmed ribosomal frameshift assay
- QUANTIFICATION AND STATISTICAL ANALYSIS
- DATA AND CODE AVAILABILTY

AUTHOR CONTRIBUTIONS

V.B. and J.A.C. designed the experiments. V.B., C.G.A.-R., and A.G.-M. contributed toward preparation and freezing of the sample. S.C. and A.D.S. carried out image acquisition and assisted in data processing. V.B carried out focused classifications with inputs from O.v.L. Map interpretation and modeling was carried out jointly by V.B., O.v.L., S.K.N., and B.P.K. H.-R.H performed bioinformatic analysis. G.B. generated the uS19 mutant cell lines. The manuscript was written by V.B., J.A.C., and B.P.K. with inputs from all other authors.

SUPPORTING CITATIONS

The following references appear in the Supplemental Information: Hedges et al. (2006); Kumar and Hedges (2011); Kumar et al. (2017).

REFERENCES

Adams, P.D., Afonine, P.V., Bunkóczi, G., Chen, V.B., Davis, I.W., Echols, N., Headd, J.J., Hung, L.-W., Kapral, G.J., Grosse-Kunstleve, R.W., et al. (2010). PHENIX: a comprehensive Python-based system for macromolecular structure solution. Acta Crystallogr. D Biol. Crystallogr. 66, 213–221.

Agrawal, R.K., Heagle, A.B., Penczek, P., Grassucci, R.A., and Frank, J. (1999). EF-G-dependent GTP hydrolysis induces translocation accompanied by large conformational changes in the 70S ribosome. Nat. Struct. Biol. 6, 643–647.

Anger, A.M., Armache, J.-P., Berninghausen, O., Habeck, M., Subklewe, M., Wilson, D.N., and Beckmann, R. (2013). Structures of the human and Drosophila 80S ribosome. Nature 497, 80–85.

Behrmann, E., Loerke, J., Budkevich, T.V., Yamamoto, K., Schmidt, A., Penczek, P.A., Vos, M.R., Bürger, J., Mielke, T., Scheerer, P., and Spahn, C.M.T. (2015). Structural snapshots of actively translating human ribosomes. Cell 161, 845–857.

Blanchard, S.C., Gonzalez, R.L., Kim, H.D., Chu, S., and Puglisi, J.D. (2004a). tRNA selection and kinetic proofreading in translation. Nat. Struct. Mol. Biol. 11, 1008–1014.

Blanchard, S.C., Kim, H.D., Gonzalez, R.L., Jr., Puglisi, J.D., and Chu, S. (2004b). tRNA dynamics on the ribosome during translation. Proc. Natl. Acad. Sci. USA 101, 12893–12898.

Bowen, A.M., Musalgaonkar, S., Moomau, C.A., Gulay, S.P., Mirvis, M., and Dinman, J.D. (2015). Ribosomal protein uS19 mutants reveal its role in coordinating ribosome structure and function. Translation (Austin) 3, e1117703.

Bretones, G., Álvarez, M.G., Arango, J.R., Rodríguez, D., Nadeu, F., Prado, M.A., Valdés-Mas, R., Puente, D.A., Paulo, J.A., Delgado, J., et al. (2018). Altered patterns of global protein synthesis and translational fidelity in RPS15-mutated chronic lymphocytic leukemia. Blood 132, 2375–2388.

Budkevich, T.V., Giesebrecht, J., Behrmann, E., Loerke, J., Ramrath, D.J.F., Mielke, T., Ismer, J., Hildebrand, P.W., Tung, C.-S., Nierhaus, K.H., et al. (2014). Regulation of the mammalian elongation cycle by subunit rolling: a eukaryotic-specific ribosome rearrangement. Cell 158, 121–131.

Cornish, P.V., Ermolenko, D.N., Noller, H.F., and Ha, T. (2008). Spontaneous intersubunit rotation in single ribosomes. Mol. Cell 30, 578–588.

Emsley, P., Lohkamp, B., Scott, W.G., and Cowtan, K. (2010). Features and development of Coot. Acta Crystallogr. D Biol. Crystallogr. 66, 486–501.

Ferguson, A., Wang, L., Altman, R.B., Terry, D.S., Juette, M.F., Burnett, B.J., Alejo, J.L., Dass, R.A., Parks, M.M., Vincent, C.T., and Blanchard, S.C. (2015). Functional Dynamics within the Human Ribosome Regulate the Rate of Active Protein Synthesis. Mol. Cell 60, 475–486.

Frank, J., and Agrawal, R.K. (2000). A ratchet-like inter-subunit reorganization of the ribosome during translocation. Nature 406, 318–322.

Green, R., and Noller, H.F. (1997). Ribosomes and translation. Annu. Rev. Biochem. *66*, 679–716.

Grimm, J.B., English, B.P., Chen, J., Slaughter, J.P., Zhang, Z., Revyakin, A., Patel, R., Macklin, J.J., Normanno, D., Singer, R.H., et al. (2015). A general method to improve fluorophores for live-cell and single-molecule microscopy. Nat. Methods *12*, 244–250.

Harger, J.W., and Dinman, J.D. (2003). An *in vivo* dual-luciferase assay system for studying translational recoding in the yeast Saccharomyces cerevisiae. RNA *9*, 1019–1024.

Hedges, S.B., Dudley, J., and Kumar, S. (2006). TimeTree: a public knowledge-base of divergence times among organisms. Bioinformatics *22*, 2971–2972.

Jacks, T., Power, M.D., Masiarz, F.R., Luciw, P.A., Barr, P.J., and Varmus, H.E. (1988). Characterization of ribosomal frameshifting in HIV-1 gag-pol expression. Nature *331*, 280–283.

Jenner, L., Demeshkina, N., Yusupova, G., and Yusupov, M. (2010). Structural rearrangements of the ribosome at the tRNA proofreading step. Nat. Struct. Mol. Biol. *17*, 1072–1078.

Khatter, H., Myasnikov, A.G., Natchiar, S.K., and Klaholz, B.P. (2015). Structure of the human 80S ribosome. Nature *520*, 640–645.

Kucukelbir, A., Sigworth, F.J., and Tagare, H.D. (2014). Quantifying the local resolution of cryo-EM density maps. Nat. Methods *11*, 63–65.

Kumar, S., and Hedges, S.B. (2011). TimeTree2: species divergence times on the iPhone. Bioinformatics *27*, 2023–2024.

Kumar, S., Stecher, G., Suleski, M., and Hedges, S.B. (2017). TimeTree: A Resource for Timelines, Timetrees, and Divergence Times. Mol. Biol. Evol. *34*, 1812–1819.

Kurian, L., Palanimurugan, R., Gödderz, D., and Dohmen, R.J. (2011). Polyamine sensing by nascent ornithine decarboxylase antizyme stimulates decoding of its mRNA. Nature *477*, 490–494.

Landau, D.A., Tausch, E., Taylor-Weiner, A.N., Stewart, C., Reiter, J.G., Bahlo, J., Kluth, S., Bozic, I., Lawrence, M., Böttcher, S., et al. (2015). Mutations driving CLL and their evolution in progression and relapse. Nature *526*, 525–530.

Li, W., Agirrezabala, X., Lei, J., Bouakaz, L., Brunelle, J.L., Ortiz-Meoz, R.F., Green, R., Sanyal, S., Ehrenberg, M., and Frank, J. (2008). Recognition of aminoacyl-tRNA: a common molecular mechanism revealed by cryo-EM. EMBO J. *27*, 3322–3331.

Ljungström, V., Cortese, D., Young, E., Pandzic, T., Mansouri, L., Plevova, K., Ntoufa, S., Baliakas, P., Clifford, R., Sutton, L.-A., et al. (2016). Whole-exome sequencing in relapsing chronic lymphocytic leukemia: clinical impact of recurrent RPS15 mutations. Blood *127*, 1007–1016.

von Loeffelholz, O., Natchiar, S.K., Djabeur, N., Myasnikov, A.G., Kratzat, H., Ménétret, J.-F., Hazemann, I., and Klaholz, B.P. (2017). Focused classification and refinement in high-resolution cryo-EM structural analysis of ribosome complexes. Curr. Opin. Struct. Biol. *46*, 140–148.

Martin, I., Kim, J.W., Lee, B.D., Kang, H.C., Xu, J.-C., Jia, H., Stankowski, J., Kim, M.-S., Zhong, J., Kumar, M., et al. (2014). Ribosomal protein s15 phosphorylation mediates LRRK2 neurodegeneration in Parkinson's disease. Cell *157*, 472–485.

Matsufuji, S., Matsufuji, T., Miyazaki, Y., Murakami, Y., Atkins, J.F., Gesteland, R.F., and Hayashi, S. (1995). Autoregulatory frameshifting in decoding mammalian ornithine decarboxylase antizyme. Cell *80*, 51–60.

Moazed, D., and Noller, H.F. (1989). Intermediate states in the movement of transfer RNA in the ribosome. Nature *342*, 142–148.

Myasnikov, A.G., Kundhavai Natchiar, S., Nebout, M., Hazemann, I., Imbert, V., Khatter, H., Peyron, J.-F., and Klaholz, B.P. (2016). Structure-function insights reveal the human ribosome as a cancer target for antibiotics. Nat. Commun. *7*, 12856.

Natchiar, S.K., Myasnikov, A.G., Kratzat, H., Hazemann, I., and Klaholz, B.P. (2017). Visualization of chemical modifications in the human 80S ribosome structure. Nature *551*, 472–477.

Pape, T., Wintermeyer, W., and Rodnina, M.V. (1998). Complete kinetic mechanism of elongation factor Tu-dependent binding of aminoacyl-tRNA to the A site of the *E. coli* ribosome. EMBO J. *17*, 7490–7497.

Pettersen, E.F., Goddard, T.D., Huang, C.C., Couch, G.S., Greenblatt, D.M., Meng, E.C., and Ferrin, T.E. (2004). UCSF Chimera—a visualization system for exploratory research and analysis. J. Comput. Chem. *25*, 1605–1612.

Pisarev, A.V., Kolupaeva, V.G., Yusupov, M.M., Hellen, C.U.T., and Pestova, T.V. (2008). Ribosomal position and contacts of mRNA in eukaryotic translation initiation complexes. EMBO J. *27*, 1609–1621.

Rodnina, M.V., and Wintermeyer, W. (2001a). Fidelity of aminoacyl-tRNA selection on the ribosome: kinetic and structural mechanisms. Annu. Rev. Biochem. *70*, 415–435.

Rodnina, M.V., and Wintermeyer, W. (2001b). Ribosome fidelity: tRNA discrimination, proofreading and induced fit. Trends Biochem. Sci. *26*, 124–130.

Rodnina, M.V., Savelsbergh, A., Katunin, V.I., and Wintermeyer, W. (1997). Hydrolysis of GTP by elongation factor G drives tRNA movement on the ribosome. Nature *385*, 37–41.

Scheres, S.H.W. (2012). RELION: implementation of a Bayesian approach to cryo-EM structure determination. J. Struct. Biol. *180*, 519–530.

Schmeing, T.M., Voorhees, R.M., Kelley, A.C., Gao, Y.-G., Murphy, F.V., 4th, Weir, J.R., and Ramakrishnan, V. (2009). The crystal structure of the ribosome bound to EF-Tu and aminoacyl-tRNA. Science *326*, 688–694.

Selmer, M., Dunham, C.M., Murphy, F.V., IV, Weixlbaumer, A., Petry, S., Kelley, A.C., Weir, J.R., and Ramakrishnan, V. (2006). Structure of the 70S ribosome complexed with mRNA and tRNA. Science *313*, 1935–1942.

Shao, S., Murray, J., Brown, A., Taunton, J., Ramakrishnan, V., and Hegde, R.S. (2016). Decoding Mammalian Ribosome-mRNA States by Translational GTPase Complexes. Cell *167*, 1229–1240.e15.

Spahn, C.M.T., Gomez-Lorenzo, M.G., Grassucci, R.A., Jørgensen, R., Andersen, G.R., Beckmann, R., Penczek, P.A., Ballesta, J.P.G., and Frank, J. (2004). Domain movements of elongation factor eEF2 and the eukaryotic 80S ribosome facilitate tRNA translocation. EMBO J. *23*, 1008–1019.

Spiegel, P.C., Ermolenko, D.N., and Noller, H.F. (2007). Elongation factor G stabilizes the hybrid-state conformation of the 70S ribosome. RNA *13*, 1473–1482.

Stark, H., Orlova, E.V., Rinke-Appel, J., Jünke, N., Mueller, F., Rodnina, M., Wintermeyer, W., Brimacombe, R., and van Heel, M. (1997). Arrangement of tRNAs in pre- and posttranslational ribosomes revealed by electron cryomicroscopy. Cell *88*, 19–28.

Valle, M., Zavialov, A., Sengupta, J., Rawat, U., Ehrenberg, M., and Frank, J. (2003). Locking and unlocking of ribosomal motions. Cell *114*, 123–134.

Voorhees, R.M., Weixlbaumer, A., Loakes, D., Kelley, A.C., and Ramakrishnan, V. (2009). Insights into substrate stabilization from snapshots of the peptidyl transferase center of the intact 70S ribosome. Nat. Struct. Mol. Biol. *16*, 528–533.

Voorhees, R.M., Schmeing, T.M., Kelley, A.C., and Ramakrishnan, V. (2010). The mechanism for activation of GTP hydrolysis on the ribosome. Science *330*, 835–838.

Voorhees, R.M., Fernández, I.S., Scheres, S.H.W., and Hegde, R.S. (2014). Structure of the mammalian ribosome-Sec61 complex to 3.4 Å resolution. Cell *157*, 1632–1643.

Whitford, P.C., Geggier, P., Altman, R.B., Blanchard, S.C., Onuchic, J.N., and Sanbonmatsu, K.Y. (2010). Accommodation of aminoacyl-tRNA into the ribosome involves reversible excursions along multiple pathways. RNA *16*, 1196–1204.

Wintermeyer, W., and Rodnina, M.V. (2000). Translational elongation factor G: a GTP-driven motor of the ribosome. Essays Biochem. *35*, 117–129.

Wohlgemuth, I., Pohl, C., and Rodnina, M.V. (2010). Optimization of speed and accuracy of decoding in translation. EMBO J. *29*, 3701–3709.

Yu, L., Kim, H.T., Kasar, S., Benien, P., Du, W., Hoang, K., Aw, A., Tesar, B., Improgo, R., Fernandes, S., et al. (2017). Survival of Del17p CLL Depends

on Genomic Complexity and Somatic Mutation. Clin. Cancer Res. *23*, 735–745.

Zaher, H.S., and Green, R. (2009). Fidelity at the molecular level: lessons from protein synthesis. Cell *136*, 746–762.

Zhang, K. (2016). Gctf: Real-time CTF determination and correction. J. Struct. Biol. *193*, 1–12.

Zheng, S.Q., Palovcak, E., Armache, J.-P., Verba, K.A., Cheng, Y., and Agard, D.A. (2017). MotionCor2: anisotropic correction of beam-induced motion for improved cryo-electron microscopy. Nat. Methods *14*, 331–332.

Zhou, J., Lancaster, L., Donohue, J.P., and Noller, H.F. (2019). Spontaneous ribosomal translocation of mRNA and tRNAs into a chimeric hybrid state. Proc. Natl. Acad. Sci. USA *116*, 7813–7818.

STAR★METHODS

KEY RESOURCES TABLE

REAGENT or RESOURCE	SOURCE	IDENTIFIER
Chemicals, Peptides, and Recombinant Proteins		
Pierce Anti-HA Magnetic Beads	Thermo Fisher Scientific	88836
HA Synthetic Peptide	Thermo Fisher Scientific	26184
Cycloheximide	Sigma-Aldrich	C4859-1ML
Puromycin	Invivogen	ant-pr-5
Protease Inhibitor Cocktail (EDTA-Free, mini-Tablet)	Bimake	B14012
RNaseout	Invitrogen	10777-019
RNasin	Promega	N251
Spermidine	Sigma-Aldrich	S2626-1G
FreeStyle 293 Expression Medium	Thermo Fisher Scientific	12338026
293fectin Transfection Reagent	Thermo Fisher Scientific	12347019
Lipofectamine 2000 Transfection Reagent	Thermo Fisher Scientific	11668019
JF646 HaloTag Ligand	Grimm et al., 2015	N/A
Deposited Data		
Cryo-EM map of classical-PRE state ribosome	This Paper	EMD-10668
Cryo-EM map of hybrid-PRE state ribosome	This Paper	EMD-10690
Cryo-EM map of POST state ribosome	This Paper	EMD-10674
Atomic model of classical-PRE state ribosome	This Paper	6Y0G
Atomic model of hybrid-PRE state ribosome	This Paper	6Y57
Atomic model of POST state ribosome	This Paper	6Y2L
Experimental Models: Cell Lines		
HEK Expi293F cells	Thermo Fisher Scientific	A14527
HEK293T-uS19 Gly 134 Arg cell line	Bretones et al., 2018	N/A
HEK293T-uS19 Thr 136 Ala cell line	Bretones et al., 2018	N/A
HEK293T-uS19 Lys 145 Asn cell line	Bretones et al., 2018	N/A
Recombinant DNA		
HA-tagged Fmr1 Fl	This Paper	N/A
Halo-Linker-mCherry	This Paper	N/A
Halo-Linker-HIV-PRF-1-mCherry	This Paper	N/A
Halo-Linker-Antizyme1-PRF-mCherry	This Paper	N/A
Software and Algorithms		
Ape - A plasmid Editor	Utah	https://jorgensen.biology.utah.edu/wayned/ape/
CryoFLARE	In house (A. D. S)	www.cryoflare.org
Relion 2.1	MRC-LMB	https://www3.mrc-lmb.cam.ac.uk/relion//index.php?title=Main_Page
ResMap	Kucukelbir et al., 2014	http://resmap.sourceforge.net
Phenix 1.16	Adams et al., 2010	phenix-online.org
Coot	MRC-LMB	https://www2.mrc-lmb.cam.ac.uk/personal/pemsley/coot/
Chimera	UCSF	https://www.cgl.ucsf.edu/chimera/
Pymol	Schrödinger	https://pymol.org/2/

LEAD CONTACT AND MATERIALS AVAILABILITY

Further information and requests for resources and reagents generated in this study should be directed to and will be fulfilled by the Lead Contact, Jeffrey Chao (jeffrey.chao@fmi.ch). All unique/stable reagents generated in this study are available from the Lead Contact with a completed Materials Transfer Agreement.

EXPERIMENTAL MODEL AND SUBJECT DETAILS

Adherent HEK293T cells were maintained in DMEM supplemented with 10% FBS and penicillin and streptomycin. Suspension HEK expi293F cells were grown on FreeStyle media (Thermo Fischer Scientific).

METHOD DETAILS

Sample preparation

Adherent HEK293T cells were transfected with 45 μg HA-tagged Fmr1 plasmid per 15 cm dish using 175 μL of Lipofectamine 2000 (Thermo Fischer Scientific). Suspension HEK expi293F cells were transfected with 1 μg of HA-tagged Fmr1 per milliliter of culture using 293fectin (Thermo Fischer Scientific). After 44 h of transfection, cells were treated with puromycin to a final concentration of 100 μg/mL. The cells were lysed in buffer A (50 mM Tris 7.6, 80 mM Potassium acetate, 5 mM Magnesium chloride, 2 mM 2-mercapto ethanol, RNaseout, Protease inhibitor tablet (Bimake), 1 mM Spermidine and 100 μg/mL Cycloheximide) containing 0.5% NP40. The lysate was cleared and was incubated with anti-HA beads (Thermo Fischer Scientific) for 4 h with mixing at 4°C. The beads were washed 2X with buffer A and subsequently eluted with buffer A containing 2 mg/mL HA-peptide (Thermo Fischer Scientific). 400 μL of the elution was then spun down at 100000 g for 40 minutes at 4°C in S120-AT2 rotor (Thermo Fischer Scientific). The ribosomal pellet was then resuspended in resuspension buffer (50 mM HEPES 7.6, 80 mM Potassium acetate, 5 mM Magnesium chloride, 1 mM DTT and 100 μg/mL cycloheximide) to get a final concentration of ribosomes at 1 mg/mL. 4 μL of the sample was applied on the Quantifoil R2/2 Cu 300 mesh grids (Quantifoil, Micro Tools GmbH, Germany). The grids were blotted for 3 s at 4°C and 80% humidity and subsequently plunge frozen in liquid ethane using Leica EM GP plunge freezer (Leica Microsystems, Germany).

Image acquisition and data processing

Cryo-EM data were acquired on a C_s-corrected (CEOS GmbH, Heidelberg, Germany) FEI Titan Krios microscope (Thermo Fischer Scientific) operated at 300 kV equipped with a Gatan-K2 Summit direct detector (operated in counting mode) (Gatan Inc., USA) and Quantum-LS Gatan Image Filter (GIF, slit width of 20 eV). A total of 8942 micrographs recorded as movies (40 frames/micrograph) were acquired in three different datasets at a calibrated magnification of 58140x (corresponding to 0.86 Å/pixel) using the previously published atomic model of the human ribosome (PDB: 6QZP; Natchiar et al., 2017) with a defocus range of 0.5 to 2.5 μm. For the first dataset, 2536 micrographs were recorded with a dose of 35.7 e⁻/Å². For the second dataset, 941 micrographs were recorded with a dose of 40.4 e⁻/Å². For the third dataset, 5465 images were recorded with a dose of 32.4 e⁻/Å². CryoFLARE (www.cryoflare.org, developed in house) was used for automation of initial micrograph processing. CryoFLARE automates initial processing by combining MotionCor2, Gctf and Gautomatch for drift-correction and dose-weighting, CTF determination and particle picking (550 × 550 box size), respectively (Zhang, 2016; Zheng et al., 2017). All further processing was carried out in RELION-2.1 (Scheres, 2012). Initial 2D classification was performed for each dataset individually. Subsequently, the good particles were merged and used for initial 3D refinement. After the 3D initial refinement, multiple rounds of 3D classification were performed including an initial unsupervised classification followed by masked 3D classifications and refinement (von Loeffelholz et al., 2017) (Figure S1). For the masked classifications, the map segmentation was done in UCSF Chimera for obtaining the density for the region of choice followed by generation of the binary mask in RELION-2.1 (von Loeffelholz et al., 2017; Pettersen et al., 2004; Scheres, 2012). Subsequently, particles belonging to specific conformation of ribosomes were refined. The resolution estimates of the maps are based on the Fourier Shell Correlation (FSC) curve at the 0.143 criterion, calculated using two half datasets. The final maps were corrected for the modulation transfer function (MFT) of the K2 camera and sharpened by a B-factor automatically determined in RELION-2.1 (Scheres, 2012). The map was subsequently low-pass filtered with the resolution cut-off corresponding to the FSC value of 0.143 and was used for model building. The variation in the local resolution for each map was calculated from the two independent half maps generated during refinement using ResMap (Kucukelbir et al., 2014).

Refinement and model building

The previously published structure of the human ribosome (PDB: 5LKS) (Myasnikov et al., 2016) and (PDB: 6QZP) (Natchiar et al., 2017) was chosen as the initial atomic model for the refinement. Since we isolated translating ribosomes, it is likely that the observed densities for the mRNA and tRNAs are averaged over multiple different species. For modeling purposes, we used the tRNA and mRNA models from the PDB 5AJ0 (Behrmann et al., 2015) and 3J7R (Voorhees et al., 2014). This initial model was docked into the map using UCSF Chimera and was subjected to initial round of rigid body refinement, and real-space refinement with global minimization, local grid search, simulated annealing and ADP (B-factor) refinement using real-space refine in PHENIX suite (Adams et al.,

2010; Pettersen et al., 2004). This refined model was inspected and manipulated in coot and subjected to real-space refinement with global minimization, local grid search, and ADP (B-factor) refinement in PHENIX suite (Adams et al., 2010; Emsley et al., 2010). Parts of model that were not present in the initial refined model were built in coot including the uS19 C-terminal tail and was subjected to real-space refinement as mentioned above. This process of building and refinement was done iteratively. The model was subjected to a final round of real-space refinement with global minimization, local grid search, and ADP (B-factor) refinement to obtain the final model (Adams et al., 2010). Despite the initial purification using HA-Fmr1, density for Fmr1 was not observed in any of the ribosome conformations we obtained suggesting that it may have been lost during subsequent stages of purification or freezing. Figures were prepared using the UCSF Chimera (Pettersen et al., 2004) and Pymol (The PyMOL Molecular Graphics System, Version 2.0 Schrödinger, LLC) software. The color nomenclature used in figure legends are based on Pymol (except for Figures S3A). Analysis of the interface was done using 'Protein interfaces, surfaces and assemblies' service PISA at the European Bioinformatics Institute. (https://www.ebi.ac.uk/pdbe/prot_int/pistart.html).

Programmed ribosomal frameshift assay
HEK293T wild-type and mutant cells (uS19- G134R, T136A and K145N cells (Bretones et al., 2018)) were seeded in a 12-well plate in antibiotic free DMEM supplemented with 10% FBS. The dual-fluorescent reporter plasmids (0.5 µg) were transfected in these cells using Lipofectamine 2000. After 5 h of transfection, the cells were trypsinized and seeded in a new 12-well plate. The fraction of single and of dual positive fluorescent cells was calculated after 24 h of transfection by fluorescent flow cytometry.

QUANTIFICATION AND STATISTICAL ANALYSIS

A total of 30,000 events in fluorescent flow cytometry are used to calculate the percentage of single (Halo) and of dual-positive fluorescent cells (Halo and mCherry). Fraction of dual-positive cells were calculated by dividing mCherry positive cells by Halo positive cells. Further, fraction of dual-positive cells in all conditions were normalized to the fraction of dual-positive cells in the wild-type cells which is shown as the normalized fold change in PRF. The results of PRF assay were evaluated using the Student's t test. A p value of < 0.05 (single asterisk) and < 0.01 (double asterisk) are considered to be significant.

DATA AND CODE AVAILABILTY

The cryo-EM maps and the corresponding atomic models for the classical-PRE, hybrid-PRE and POST state human ribosomes generated in this study are submitted to the electron microscopy databank and the protein databank with accession numbers EMD-10668 and 6Y0G, EMD-10690 and 6Y57, and EMD-10674 and 6Y2L, respectively.